J. Fluid Mech. (2001), *vol.* 431, *pp.* 65–89. Printed in the United Kingdom

Tangential flow and advective mixing of viscoplastic fluids between eccentric cylinders

By YURUN FAN[1,3], NHAN PHAN-THIEN[1,2] AND ROGER I. TANNER[1]

[1]Department of Mechanical and Mechatronic Engineering, The University of Sydney, NSW 2006, Australia

[2]Department of Mechanical Engineering, The University of Singapore, Singapore 119260

[3]State Key Laboratory of Fluid Power Control and Transmission, Zhejiang University, 310027 China

(Received 17 June 1999 and in revised form 28 August 2000)

This is a study on the tangential flow and advective mixing of viscoplastic fluids (Bingham plastics) between two eccentric, alternately rotating cylinders. Two geometrical configurations and various rotation modes are considered for a relatively large range of the yield stress. The *hp*-type finite element method with the mixed formulation is used to solve for the steady velocity and pressure fields. The bi-viscosity and the Papanastasiou models agree quantitatively with each other in predicting the velocity fields and the practically unyielded zones. However, the Papanastasiou model is more robust and economic than the bi-viscosity model in the computation using Newton iteration. In the steady flows, in addition to the motionless zones, we have discovered some plugs with rigid rotation, including rotating plugs stuck onto the outer cylinder and rotating, even counter-rotating, plugs disconnected from both cylinders. The unsteady, periodic flow is composed of a sequence of the steady flows, which is valid in the creeping flow regime. The characteristics of advective mixing in these flows have been studied by analysing the asymptotic coverages of a passive tracer, the distributions of the lineal stretching in the flow and the variations of the mean stretching of the flow with time. The tracer coverage is intuitive but qualitative and, occasionally, it depends on the initial location of the tracer. On the other hand, the distribution of stretching is quantitative and more reliable in reflecting the mixing characteristics. Interestingly, the zones of the lowest stretching in the distribution graphs are remarkably well matched with the regular zones in the tracer-coverage graphs. Furthermore, the mixing efficiency proposed by Ottino (1989) is used to characterize the advective mixing in the two geometrical configurations with various rotation modes. It is important to realize that, for plastic fluids, a major barrier to effective mixing is the unyielded fluid plugs which are controlled by the yield stress and geometrical configurations. Therefore, when designing an eccentric helical annular mixer it is important to pay attention first to the geometric issues then to the operating issues.

1. Introduction

Many fluids of engineering interest appear to exhibit yield behaviour, where flow occurs only when the imposed stress exceeds a critical yield stress level. Such materials,

often called Bingham plastic fluids, are frequently encountered in industrial problems; they include greases, paints, slurries, pastes, suspensions and foodstuff such as dough, cheese and mayonnaise. It is thus not surprising to find that mixing of yield-stress fluids is common in practice. A summary of the rheology of viscoplastic materials was given by Bird, Dai & Yarusso (1983). More recently, a thorough review of the concept of yield stress was given by Barnes (1999). Briefly, if one is interested in and is capable of measuring extremely small shear rates, then the yield stress does not exist as a physical property, i.e. '$\pi\alpha\nu\tau\alpha\ \rho\varepsilon\iota$' – everything flows; otherwise the concept of a yield stress has proved very useful in a whole range of applications once the yield stress is defined as a mathematical curve-fitting constant, used along with other parameters to produce an equation to describe the flow curve of a material over a limited range of shear rates. Since there can be strong coupling between the mixing flow and the material being mixed, it is apparent that new technological developments will necessitate a deep understanding of the chaotic mixing of fluids with complex rheology.

There are a few model mixers amenable to detailed investigations both by experimentation and computation (Ottino 1989; Kusch & Ottino 1992); one of them is the eccentric helical annular mixer (EHAM) in which a pressure-driven axial Poiseuille flow between two eccentric cylinders is perturbed by rotating the cylinders periodically in time. This mixer has a continuous input–output and, with no sharp edges, it can be designed to have mild-shear-rate histories to avoid breakage and degradation of macromolecules. The two-dimensional, chaotic mixing of viscous fluids between eccentric cylinders has been extensively analysed in the Stokes regime (Chaiken *et al.* 1987; Aref & Balachandar 1986; Swanson & Ottino 1990; Muzzio, Swanson & Ottino 1991); an excellent agreement between the experimentally observed and the theoretically predicted mixing patterns has been demonstrated by Swanson & Ottino (1990). The investigation was later extended to an experimental study on the EHAM flow, i.e. to including the axial flow, by Kusch & Ottino (1992). Their results show that although the axial flow does have an influence on the mixing structures created in the EHAM, the major feature of the streakline coverages appears to be controlled by the modulation of the cylinder rotations. Regarding the rheological effects, the experimental and computational investigations of Niederkorn & Ottino (1993, 1994) addressed the fluid elasticity and shear-thinning viscosity. The study of Souvaliotis, Jana & Ottino (1995) suggests that the accuracy requirement for the velocity field is not as stringent as the exponential stretching of chaotic mixing seems to suggest. More recently, our numerical investigation (see Fan, Tanner & Phan-Thien 2000) found that the fluid elasticity has relatively little effect on the kinematics and advective mixing in an eccentric annulus; on the other hand, the shear-thinning property has a large impact on both the kinematics and the mixing characteristics. Furthermore, the results of our fully unsteady computation indicate that the transient response of the viscoelastic fluid, caused by switching the cylinder rotations and the stress relaxation, can be neglected if only the final mixing results are of interest; thus the piecewise-steady assumption has been justified.

The present study considers the advective mixing of plastic fluids in the two-dimensional, time-periodic flows between eccentric cylinders and has two main motivations:

First, we seek to model the *tangential* plastic flow in a complex geometry, which is of wide application yet has received little attention in the literature. There have been a few investigations on the *axial* flow of Bingham plastics in eccentric annuli (Walton & Bittleston 1991; Beverly & Tanner 1992); through their work the flow pattern with a true plug was established.

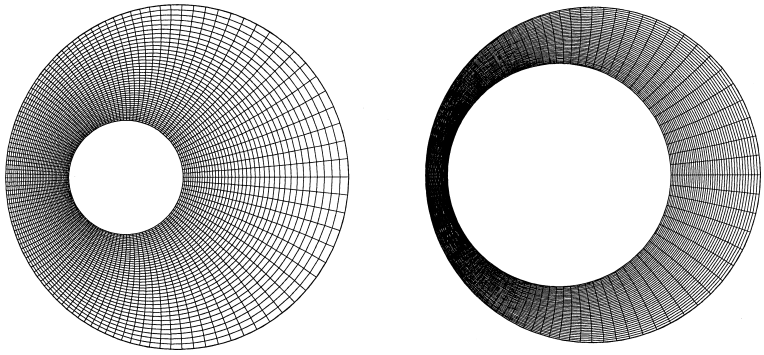

Configuration-1 : $\mu = 2.0$, $\epsilon = 0.45$ Configuration-2 : $\mu = 0.5$, $\epsilon = 0.6$

FIGURE 1. Geometrical configurations considered and the corresponding finite element meshes.

Second, since the flow patterns for plastic materials are expected to be significantly different from their counterparts for Newtonian fluids, we intend to examine the corresponding characteristics and efficiency of advective mixing in the time-periodic flow between eccentric cylinders.

We use two viscoplastic models, the bi-viscosity and Papanastasiou's, in the hp-type finite element method to solve for the steady velocity and pressure fields corresponding to each cylinder's rotation. Unyielded fluid is then detected by using the criteria implied by the models. Neglecting the fluid inertia, the unsteady flow is composed of a sequence of the steady flows. The tools used to evaluate the advective mixing include the asymptotic coverage of a passive tracer, the stretching distribution of fluid elements, the mean stretching of the flow and the mixing efficiency proposed by Ottino (1989). The present work considers two geometrical configurations, and spans a relatively large range of the yield stress and the modulation of cylinder rotation.

2. Problem definitions

The flow domain is confined between two eccentric cylinders with parallel axes displaced by a distance e. The radii of the inner and outer cylinders are R_i and R_o, respectively. The geometrical configuration is completely specified by a dimensionless gap μ and a dimensionless eccentricity ϵ which are defined as

$$\mu = \frac{R_o - R_i}{R_i}, \tag{2.1}$$

$$\epsilon = \frac{e}{R_o - R_i}. \tag{2.2}$$

Figure 1 shows the two configurations considered and the corresponding finite element meshes used in the present study. Configuration 1 with $\mu = 2.0$ and $\epsilon = 0.45$ is the same as used in the investigations of Swanson & Ottino (1990) for Newtonian fluids, and Niederkorn & Ottino (1993, 1994), and Fan *et al.* (2000) for viscoelastic and shear-thinning fluids. Configuration 2, with a smaller gap and a larger eccentricity, $\mu = 0.6$ and $\epsilon = 0.6$, was chosen because of its potential capacity for significantly reducing the unyielded zones in this tangential annular flow.

Chaotic advection in eccentric annuli can be achieved by alternately rotating the inner and outer cylinders with angular velocities Ω_i and Ω_o, respectively. As long

as the creeping flow assumption is valid, the actual magnitude of the cylinder's rotation velocities is unimportant, only their *displacements* affect the fluid advection, as indicated by Swanson & Ottino (1990). As in the previous investigations, a square-wave form of the modulation is adopted, that is, at any time only one cylinder is allowed to rotate with a constant angular velocity and the change from one rotating to the other is instantaneous. In order to keep the investigation reasonably focused, we restrict ourselves to the case of *counter-rotation*, and that, in a period T, the total linear displacement of the inner cylinder is equal to that of the outer cylinder. Thus the modulation or the *rotation mode* can be characterized by the angular displacement of the outer cylinder per period:

$$\theta = \int_0^T \Omega_o \mathrm{d}t. \tag{2.3}$$

3. Models for Bingham viscoplastic fluids

The Bingham model is one of the simplest that describes fluids with yield stresses. In a simple shear flow, it is characterized by a flow curve (the shear stress versus the steady shear rate) which is a straight line having an intercept τ_y on the shear-stress axis, and it is this yield stress that must be exceeded before flow commences, the shear rate then being proportional to the excess of the stress over the yield stress. Within the unyielded region, the material flows as a rigid body while in the yielded region the material behaves as a Newtonian fluid under the influence of a shear stress equivalent to $\tau - \tau_y$. The general form of the *Bingham model* suitable for three-dimensional flows is

$$\left.\begin{aligned} \boldsymbol{\tau} &= (\eta + \tau_y/\dot{\gamma})\dot{\boldsymbol{\gamma}}, & \tau \geqslant \tau_y \\ \dot{\boldsymbol{\gamma}} &= \mathbf{0}, & \tau < \tau_y \end{aligned}\right\} \tag{3.1}$$

where η is the intrinsic viscosity of the yielded fluid, $\dot{\boldsymbol{\gamma}} = \nabla \boldsymbol{u} + (\nabla \boldsymbol{u})^T$ is the strain rate tensor, $\boldsymbol{u}$ the velocity, and $\dot{\gamma} = \sqrt{\dot{\boldsymbol{\gamma}} : \dot{\boldsymbol{\gamma}}/2}$ is the generalized strain rate (second invariant of the strain tensor), $\boldsymbol{\tau}$ is the deviatoric part of the total stress tensor $\boldsymbol{\sigma} = -p\boldsymbol{I} + \boldsymbol{\tau}$, where p is the isotropic pressure and $\boldsymbol{I}$ the unit tensor, and $\tau = \sqrt{\boldsymbol{\tau} : \boldsymbol{\tau}/2}$ is the second invariant of $\boldsymbol{\tau}$. As mentioned in the introduction, the Bingham model is an idealization of real plastic fluids. Although this constitutive relation is amenable to analytical solutions for some rectilinear flows (see Bird *et al.* 1983), it poses significant problems in the numerical simulation of complex geometries: when the strain rate approaches zero, the apparent viscosity is unbounded, and the stress becomes indeterminate in the unyielded region. To tackle this singular behaviour, some researchers prefer adding a small number to the denominator in equation (3.1) (e.g. Bercovier & Engelman 1980; Walton & Bittleston 1991); a more popular approach, however, is to introduce the *bi-viscosity* approximation:

$$\left.\begin{aligned} \boldsymbol{\tau} &= (\eta + \tau_y/\dot{\gamma})\dot{\boldsymbol{\gamma}}, & \tau \geqslant \tau_y \\ \boldsymbol{\tau} &= \eta_r \dot{\boldsymbol{\gamma}}, & \tau < \tau_y \end{aligned}\right\} \tag{3.2}$$

where η_r is a relatively large reference viscosity compared to η. The flow curve of this model can approximate the Bingham model down to a very small shear rate if sufficiently large η_r is chosen. The Newtonian behaviour of this model at small strain rates facilitates theoretical analyses of viscoplastic flows (e.g. Lipscomb & Denn 1984; Gartling & Phan-Thien 1984) and its usefulness in the numerical simulation has been confirmed by several investigations (Beverly & Tanner 1989, 1992; Nieckele, Naccache

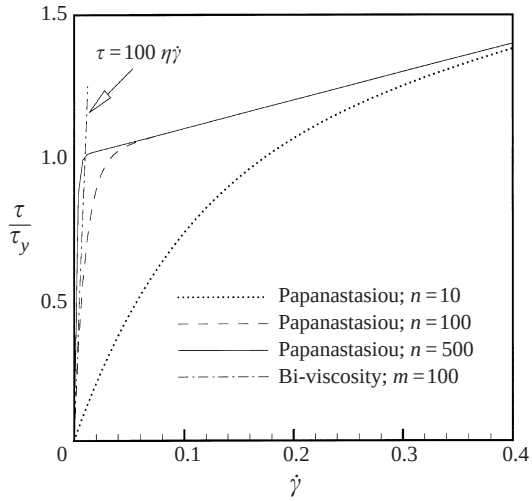

FIGURE 2. Flow curves of the Papanastasiou and bi-viscosity models.

& Mendes 1998). Another modified constitutive equation for Bingham plastics was introduced by *Papanastasiou* (1987):

$$\boldsymbol{\tau} = \left(\eta + \frac{\tau_y(1 - \exp(-n\dot{\gamma}))}{\dot{\gamma}}\right)\dot{\boldsymbol{\gamma}}. \tag{3.3}$$

Unlike the bi-viscosity model, here a single constitutive equation holds in both the yielded and unyielded regions. With a relatively large exponent n, a quick growth of the stress can be achieved at relatively very low strain rates, which is consistent with the behaviour of the material in its practically unyielded state. In the limiting case of $n \to \infty$, Papanastasiou's model reduces to the Bingham model in the yielded region. In the unyielded region,

$$\lim_{\dot{\gamma}\to 0} \boldsymbol{\tau} = (\eta + n\tau_y)\dot{\boldsymbol{\gamma}}, \tag{3.4}$$

thus the singular behaviour in the Bingham model is eliminated. Successful applications of Papanastasiou's model to the extrusion flow and to the entry and exit flows were reported by Papanastasiou (1987), Ellwood *et al.* (1990), and Abdali, Mitsoulis & Markatos (1992).

The radius and angular velocity of the inner cylinder, R_i and Ω_i, and the intrinsic viscosity η are taken as the scaling parameters. The dimensionless yield stress is defined as

$$Y = \frac{\tau_y}{\eta\Omega_i}. \tag{3.5}$$

The stress, strain rate and the parameter n in Papanastasiou's model are non-dimensionized correspondingly; the dimensionless reference viscosity in the bi-viscosity model is

$$m = \frac{\eta_r}{\eta}. \tag{3.6}$$

Figure 2 shows the flow curves predicted by the bi-viscosity and Papanastasiou's models. By taking the second invariants on both sides of equation (3.3), we can define

Y	n	$\dot{\gamma}_c$
1	100	0.03386
1	1000	0.00525
1	10000	0.00072
10	100	0.05250
10	1000	0.00723
10	10000	0.00092

TABLE 1. The critical strain rate predicted by the Papanastasiou model for some values of the yield stress and the parameter n.

the yield condition as $\tau = \tau_y$ and get a equation for the critical strain rate $\dot{\gamma}_c$,

$$\dot{\gamma}_c = Y \exp(-n\dot{\gamma}_c). \tag{3.7}$$

Table 1 gives some typical values for $\dot{\gamma}_c$, which indicate that the critical strain rate is not very sensitive to the values of the yield stress in the Papanastasiou model.

4. Finite element method

For the eccentric annulus geometry, the bipolar coordinate system is commonly preferred because of its advantage of fitting the boundaries with the coordinate lines. The transformation from the rectangular coordinates (x, y) to the bipolar coordinate system (ξ, ϕ) is defined as

$$x = \frac{a \sinh \xi}{\cosh \xi + \cos \phi}, \quad y = \frac{a \sin \xi}{\cosh \xi + \cos \phi}, \tag{4.1}$$

where a is a geometric parameter based on the eccentricity and the radii,

$$a = \frac{1}{2e}\sqrt{\left(R_i^2 + R_o^2 - e^2\right)^2 - 4R_i^2 R_o^2}. \tag{4.2}$$

In figure 1 the finite element meshes are uniform in the bipolar coordinate system.

The continuity and momentum equations for isothermal, creeping, steady flows of incompressible fluids are

$$\nabla \cdot \boldsymbol{u} = 0, \tag{4.3}$$

$$-\nabla p + \nabla \cdot \boldsymbol{\tau} = 0. \tag{4.4}$$

We adopt a straightforward adaptation of the mixed finite element method for the incompressible Newtonian flows, i.e. the velocity–pressure formulation. Let Ω be the flow domain and $\partial\Omega$ its boundary. On $\partial\Omega$, the partial boundaries $\partial\Omega_{\boldsymbol{u}}$, $\partial\Omega_N$ are identified with boundary conditions for the velocity $\boldsymbol{u}$ and the traction force $\boldsymbol{t}$, respectively. The variational formulation for the viscoplastic fluids can be stated as:

Find the set $(u, p) \in \mathscr{V} \times \mathscr{P}$ *such that*, $\forall \boldsymbol{\Phi}_{\boldsymbol{u}} \in \mathscr{V}$, $\forall \Phi_p \in \mathscr{P}$,

$$\int_\Omega (\eta_a(\boldsymbol{u})(\nabla \boldsymbol{u} + (\nabla \boldsymbol{u})^T) : \nabla \boldsymbol{\Phi}_{\boldsymbol{u}} - p \nabla \cdot \boldsymbol{\Phi}_{\boldsymbol{u}})\, \mathrm{d}\Omega = \int_{\partial\Omega_N} \boldsymbol{t} \cdot \boldsymbol{\Phi}_{\boldsymbol{u}}\, \mathrm{d}\partial\Omega, \tag{4.5}$$

$$\int_\Omega (\nabla \cdot \boldsymbol{u}) \boldsymbol{\Phi}_p\, \mathrm{d}\Omega = 0, \tag{4.6}$$

where $\mathscr{V}, \mathscr{P}$ *denote the function spaces defined on* Ω *and spanned by the basis functions* $\boldsymbol{\Phi}_{\boldsymbol{u}}, \boldsymbol{\Phi}_p$, *for the velocity and pressure, respectively.*

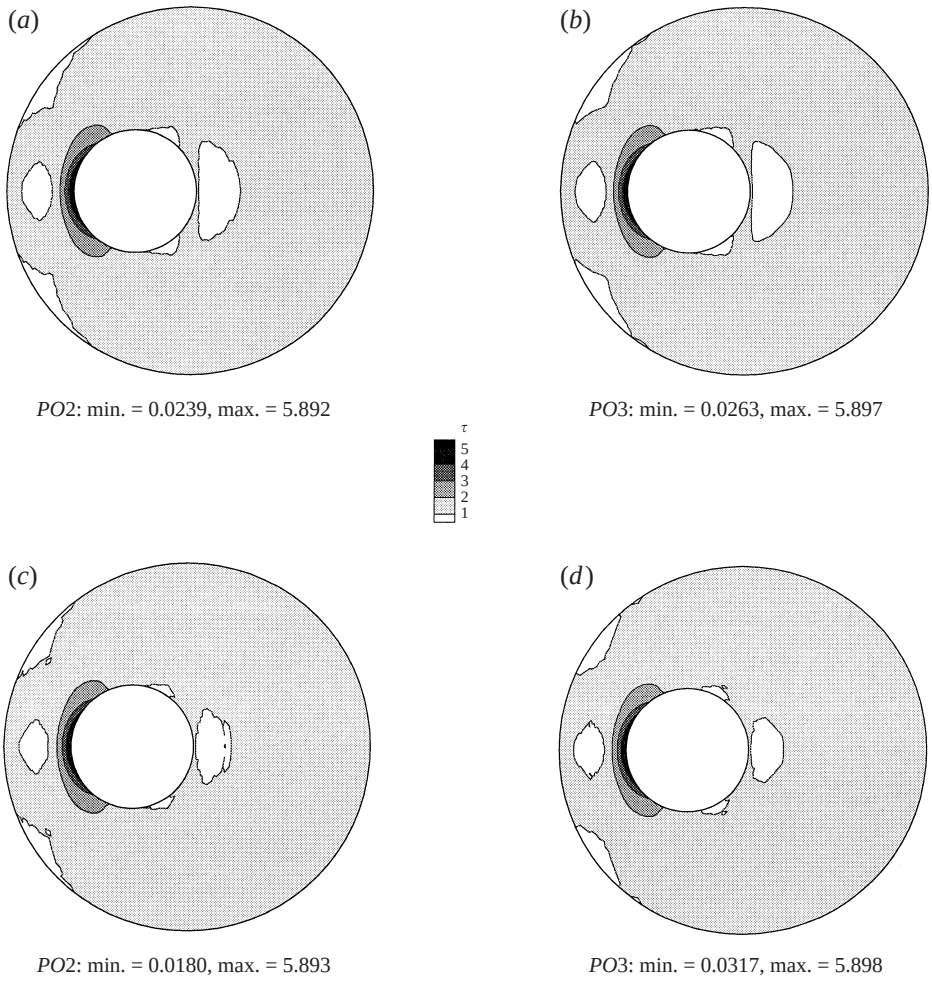

FIGURE 3. Contours of the second invariant of the extra stress $\boldsymbol{\tau}$ in configuration 1; the outer cylinder is rotating, $Y = 1.0$ and $m = 1000$, $n = 1000$ for (a, b) the Papanastasiou, and (c, d) the bi-viscosity models.

In equation (4.5), the apparent viscosity function $\eta_a(\dot{\gamma})$ is simply substituted by the bi-viscosity or the Papanastasiou viscosity through the constitutive relation:

$$\boldsymbol{\tau} = \eta_a(\dot{\gamma})\dot{\boldsymbol{\gamma}}. \tag{4.7}$$

For the basis functions of the finite element spaces, we adopted a set of hierarchic shape functions proposed by Szabo & Babuska (1991), which are particularly suitable for the implementation of increasing interpolations orders – the so-called *p*-extension. Given a finite element mesh, a discretization is specified by its interpolation order for the velocity. In the following, we mark a discretization using *PO* followed by its (highest) velocity interpolation order such as *PO*2, *PO*3 etc. The finite element discretization from equations (4.5) and (4.6) produces a set of nonlinear equations for the velocity and pressure variables; previous investigators dealing with the bi-viscosity model employed the Picard iteration to solve these equations, while here we prefer using the Newton iteration. For both the bi-viscosity and the Papanastasiou models, we found that the most efficient way to reach a required solution is to keep the yield

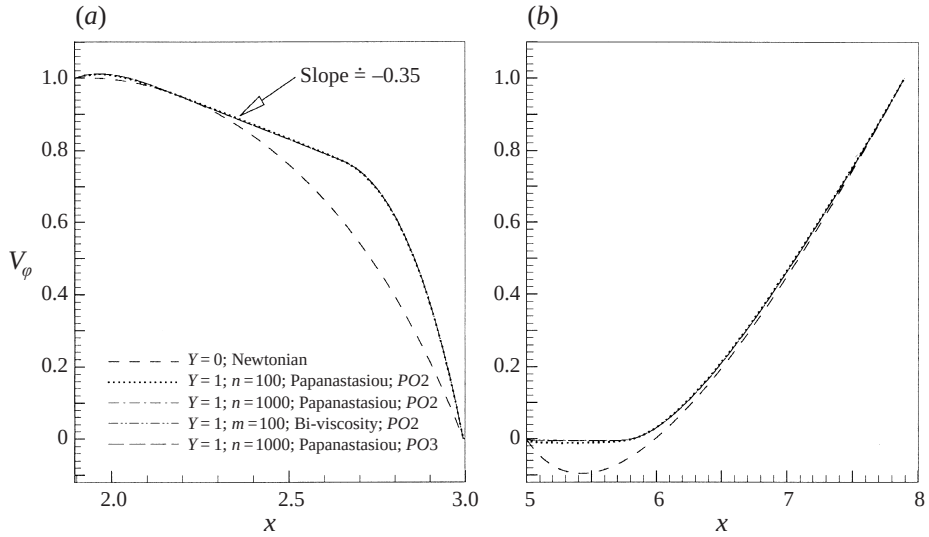

FIGURE 4. Velocity profiles of V_φ on the symmetry line for configuration 1 with the outer cylinder rotating: (*a*) small gap; (*b*) large gap.

stress Y as a chosen constant and gradually increase the parameter n or m of the model from a low value, say 1, to a designated value, say 1000. However, because the bi-viscosity function is discontinuous in its derivative, its radius of convergence is relatively very small, making the m-augmentation algorithm rather CPU time-consuming; by contrast, the Papanastasiou model, endowed with a smooth viscosity function, permits much larger steps in the n-augmentation algorithm.

5. Solutions of the steady flows

One of the major concerns in our study is the accuracy of numerical simulations because the discretization errors in the steady velocity field may be magnified exponentially in the computations for chaotic mixing (Souvaliotis *et al.* 1995). In the earlier work, Fan *et al.* (2000), we have demonstrated that, for the Newtonian creeping flow, in terms of the maximum and the root-mean-square errors with respect to the analytical solution of Wannier (1950), our p-extension computation converges and the convergence rate in terms of the number of variables solved is roughly exponential; for example, when using the discretization *PO*4, magnitudes of the maximum and the root-mean-square errors reduced to 10^{-10} and 10^{-11}, respectively.

Solution accuracy of our computation for the viscoplastic models can be assessed by examining the second invariant of the extra stress tensor, τ, which requires calculations of velocity gradients. In figure 3, contours of $\boldsymbol{\tau}$ with the yield stress $Y = 1$ are plotted. According to our criterion, the unshaded regions with $\tau \leqslant 1$ represent unyielded zones in the flow. The bi-viscosity and Papanastasiou models predict qualitatively the same unyielded zones. Changing the discretization from *PO*2 to *PO*3 does not change the flow pattern significantly, except that with the higher interpolations a smoother boundary of the unyielded zones is obtained. The variations of the minimum τ and maximum τ in these calculations seem to be insignificant. The flow characteristics can be further clarified by plotting the tangential velocity V_φ along the line connecting the centres of the cylinders as shown in figure 4. Due to the flow symmetry, the

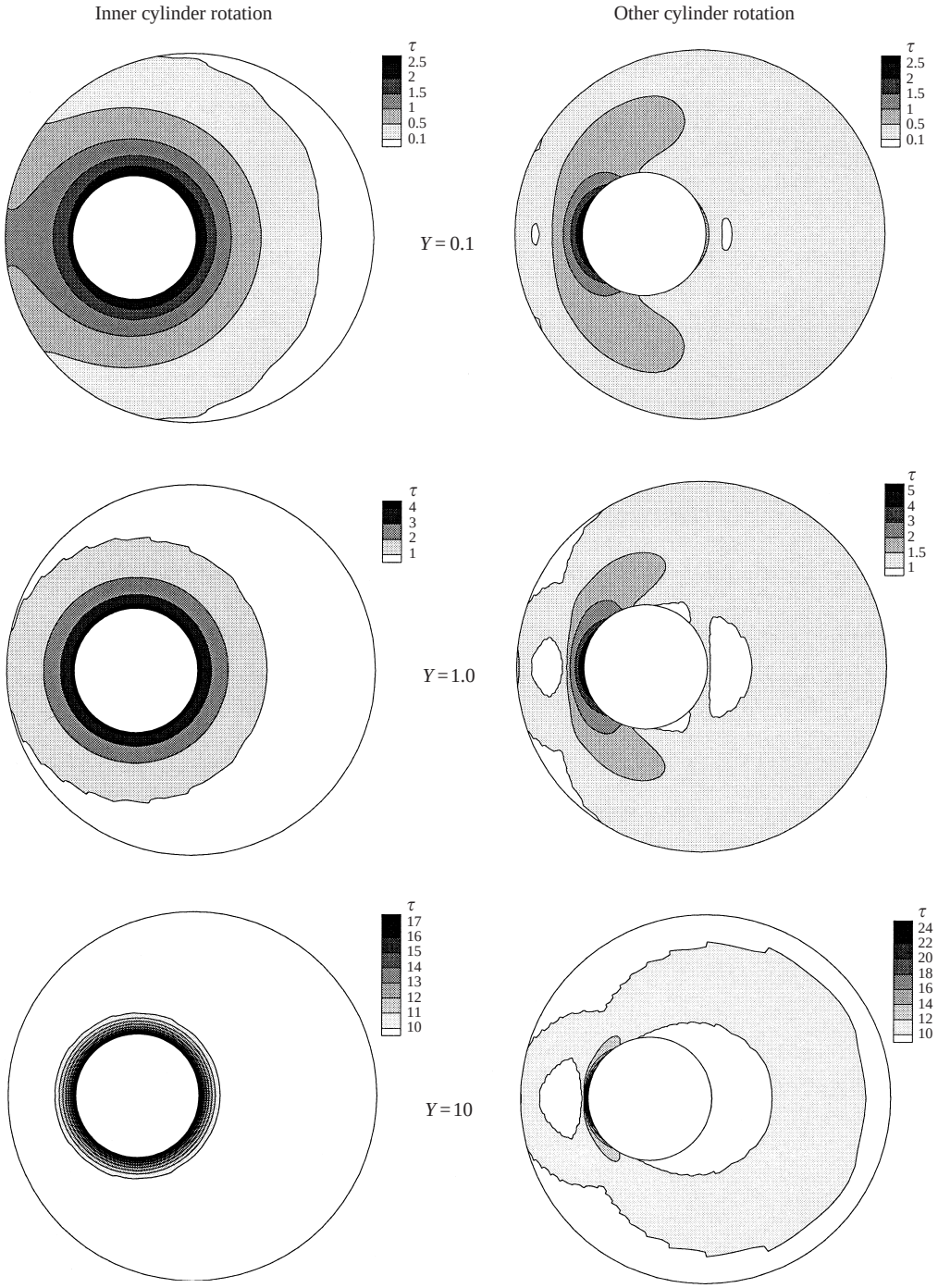

FIGURE 5. Contours of the second invariant of the extra stress $\boldsymbol{\tau}$ in configuration 1; the unyielded regions are not shaded.

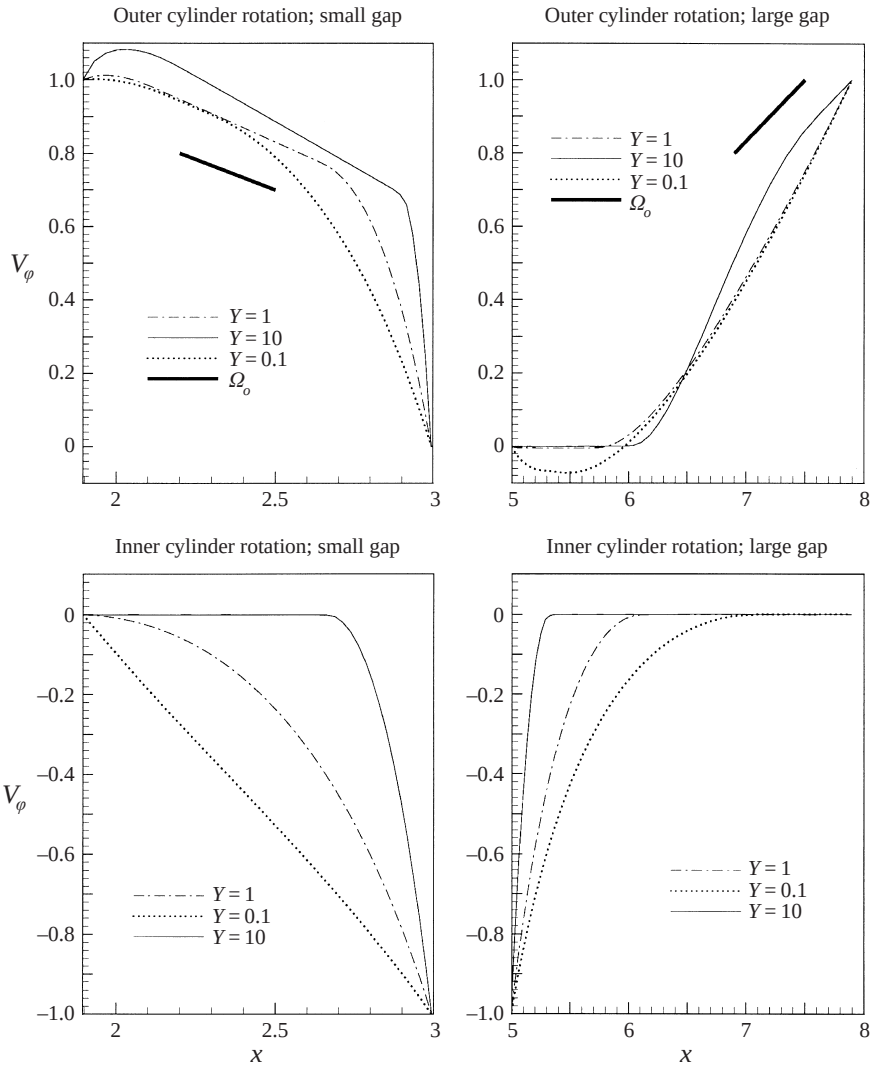

FIGURE 6. Velocity profiles of V_φ on the symmetry line in configuration 1; the thick straight line represents the velocity gradient corresponding to rigid rotation with Ω_o

radial velocity V_ξ is zero on this symmetry line. Examining figure 4, one can identify the unyielded region in the large gap of figure 3 with a dead zone; in the small gap, there is a section of a linear velocity V_φ with a slope approximately equal to -0.35; since $V_\xi = 0$, this indicates a rigid plug rotating with the angular velocity of 0.35; note that in this case the outer cylinder is rotating with the angular velocity $\Omega_o = V_o/R_o = 1/3 = 0.33$. Figure 4 also shows that the velocity profiles of the bi-viscosity model with *PO*2 and the Papanastasiou model with *PO*2 and *PO*3 cannot be distinguished visually. Furthermore, the differences in the results on changing the parameter n from 1000 to 100 are negligible.

Backed by these results, in the following we concentrate on the solutions of the Papanastasiou model with $n = 1000$ and the discretization *PO*2. Let us first consider configuration 1. Figure 5 exhibits the contours of the second invariant of the stress,

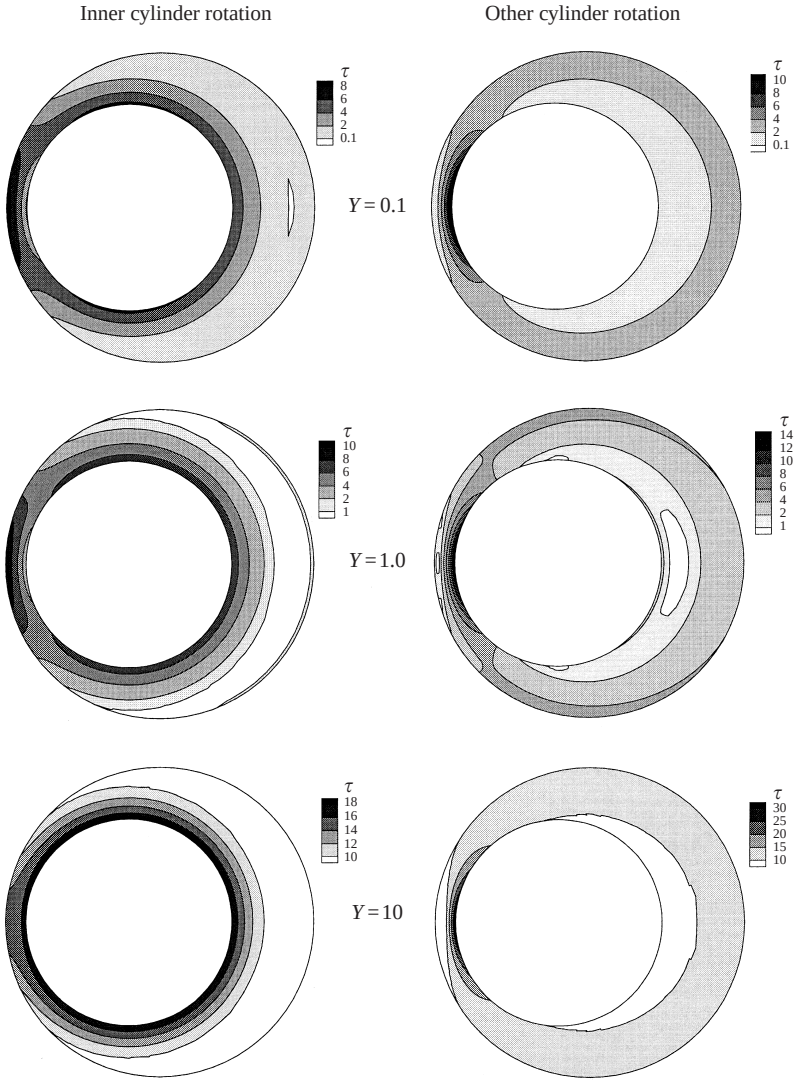

FIGURE 7. Contours of the second invariant of the extra stress $\boldsymbol{\tau}$ in configuration 2; the unyielded region is represented by the unshaded area.

τ, spanning from a weak yield stress, $Y = 0.1$, to a strong yield stress, $Y = 10$. The unyielded regions, represented by the unshaded areas, become enlarged as the corresponding yield stress increases. The character of these unyielded regions can be explained by figure 6 which, like figure 4, plots the velocity V_φ on the symmetry line. In the case of rotating outer cylinder, the range of the linear velocity profile in the small gap becomes larger and its slope steeper with higher yield stresses, indicating that more material nearby is involved in a plug-like rotation with higher angular velocities. In the large gap, a section of plug rotation stuck to the outer cylinder wall can be detected for $Y = 10$, and large dead zones stuck to the inner cylinder wall are found for $Y = 1$ and $Y = 10$. The flow patterns for the case of rotating inner cylinder are relatively simple: as the yield stress increases, the yielded region gradually shrinks to a thin layer surrounding the inner cylinder, leaving more of the outside region as motionless zone.

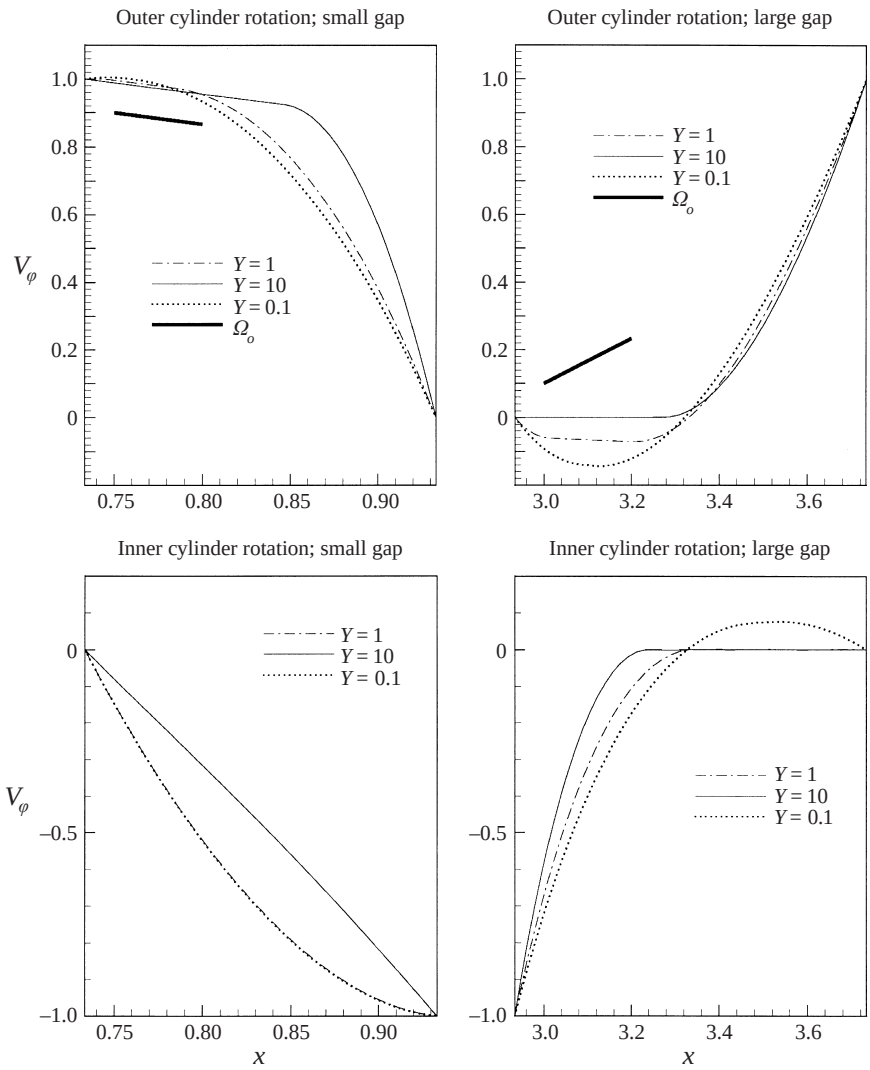

FIGURE 8. Velocity profiles of V_φ on the symmetry line in configuration 2; the thick straight line represents the velocity gradient corresponding to rigid rotation with Ω_o.

Configuration 2, with a relatively smaller gap and larger eccentricity, is expected to be able to reduce the unyielded regions observed in configuration 1, and this is confirmed by figure 7 and figure 8. For the case of rotating outer cylinder, a dead zone attached to the inner cylinder in the large gap and a plug stuck to the outer cylinder in the small gap are found for the fluid with $Y = 10$; a small plug in the small gap and a weakly rotating plug in the large gap are found for the fluid with $Y = 1$. It is interesting to notice that the plug in the large gap is *counter-rotating* with respect to the rotation of the outer cylinder. For the case of rotating inner cylinder, more and more unyielded material in the large gap sticks to the outer cylinder wall as the yield stress increases; in the small gap, the shape of the velocity profile changes from concave for $Y = 0.1$ and $Y = 1$ to a slightly convex for $Y = 10$; however, there seems little chance for the fluid to undergo a plug flow there, as can be judged by the stress

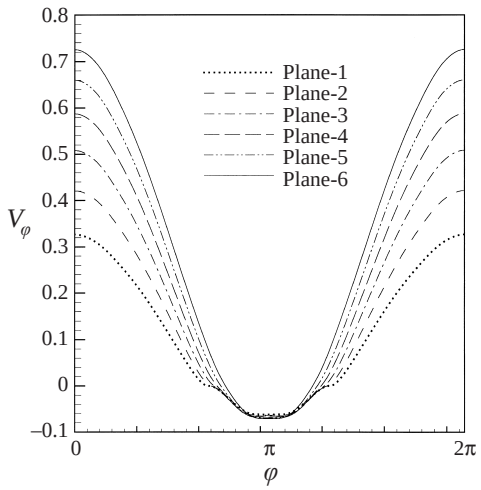

FIGURE 9. Velocity profiles of V_φ on six consecutive azimuthal lines (ξ-constant lines) passing through the counter-rotating plug in the large gap in configuration 2. Outer cylinder rotation; $Y = 1.0$.

contours in figure 7. Figure 9 provides further evidence of the counter-rotating plug in the large gap: six consecutive azimuthal lines (ξ-constant lines) are chosen to pass through the plug region and the profiles of the velocity V_φ along these lines clearly demonstrate that near the symmetry line in the large gap, $\varphi = \pi$, V_φ is negative.

Finally, we show the contours of the pressure for some cases in figure 10. All the pressure contours are symmetric with respect to the geometrical symmetry line. The contours of the Newtonian fluid are smooth, while those of the viscoplastic fluids show some apparent wiggles along the boundaries between the yielded and unyielded regions, reflecting drastic changes of the constitutive relation there.

6. Methods of computing advective mixing

In the piecewise-steady approximation, the unsteady, periodic flow is composed of two alternating steady flows corresponding to the rotation of each cylinder; the time dependence of the velocity field is periodic and discontinuous since only one cylinder is rotating at a time. One basic procedure in the computation of advective mixing is to calculate the trajectory or pathline of a fluid particle through integrating the equation of motion,

$$\frac{\mathrm{d}\boldsymbol{x}}{\mathrm{d}t} = \boldsymbol{u}(\boldsymbol{x}, t), \quad \text{with} \quad \boldsymbol{x}_{t=0} = \boldsymbol{X}, \tag{6.1}$$

where $\boldsymbol{X}$ is the initial position of a particle, $\boldsymbol{x} = \boldsymbol{x}(\boldsymbol{X}, t)$ the position at the time t, and $\boldsymbol{u}(\boldsymbol{x}, \boldsymbol{t})$ is the unsteady velocity field. Experiments on or numerical simulation of a passive tracer can provide qualitative, intuitive pictures of the mixing morphology such as the folds and striations, the regular and chaotic regions in the flow field. On the other hand, advective mixing stretches the fluid elements, enlarges the contact surfaces between different fluids and enables them to diffuse efficiently in smaller scales. In the present study, the amount of lineal stretching is used to quantitatively assess the performance of the mixing. To determine the lineal stretching let us follow a fluid element attached to an infinitesimal material vector $\mathrm{d}\boldsymbol{x}(t)$, which can be computed if

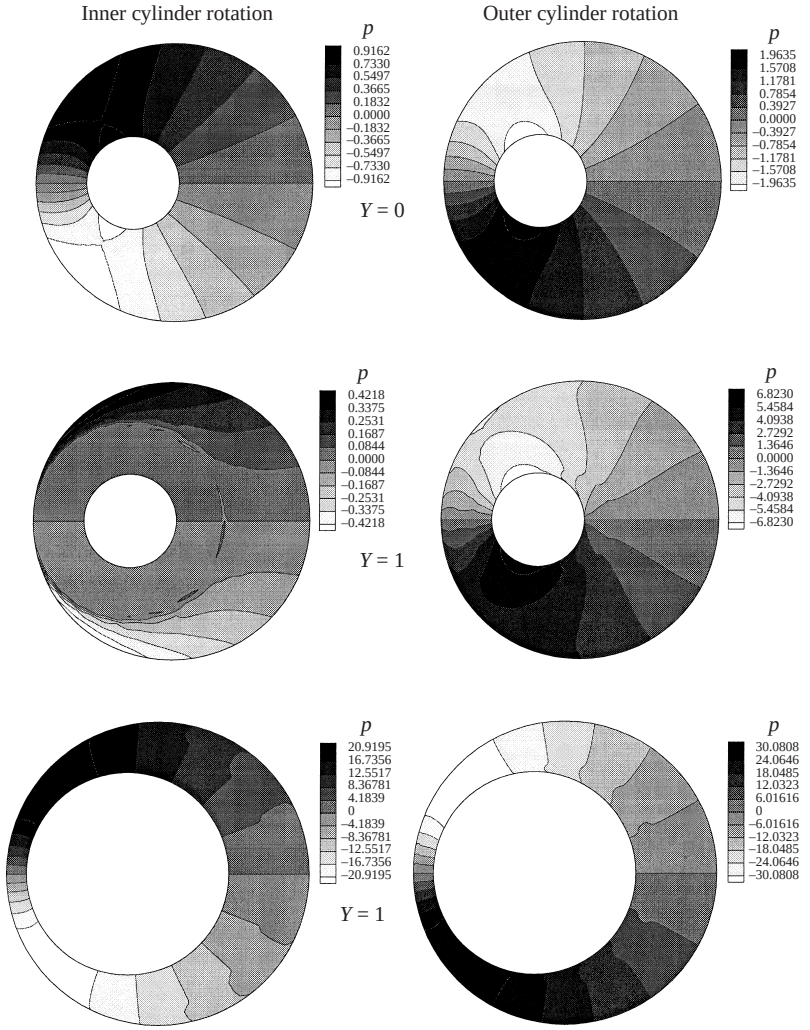

FIGURE 10. Contours of the pressure; configurations 1 (top four) and 2 (bottom 2).

we know the deformation gradient tensor, $\boldsymbol{F}$, defined as

$$\mathrm{d}\boldsymbol{x}(t) = \boldsymbol{F}(t) \cdot \mathrm{d}\boldsymbol{X}, \tag{6.2}$$

where $\mathrm{d}\boldsymbol{X}$ is the initial vector with an arbitrary orientation. This requires solving the evolution equation of the deformation gradient tensor:

$$\frac{\mathrm{d}\boldsymbol{F}}{\mathrm{d}t} = (\nabla \boldsymbol{u}(\boldsymbol{x}, t))^T \cdot \boldsymbol{F}, \quad \text{with } \boldsymbol{F}_{t=0} = \boldsymbol{I}, \tag{6.3}$$

where $\boldsymbol{I}$ is the identity tensor. Since the material vector is convected by the flow, the gradient of the velocity is time dependent even in a steady flow; therefore the equation of material position (6.1) and the equation of the deformation gradient tensor (6.3) must be solved simultaneously to obtain $\boldsymbol{x}$ and $\boldsymbol{F}$, as functions of the initial position and orientation of the material vector. The lineal stretching is defined as

$$\lambda = \frac{|\mathrm{d}\boldsymbol{x}|}{|\mathrm{d}\boldsymbol{X}|}. \tag{6.4}$$

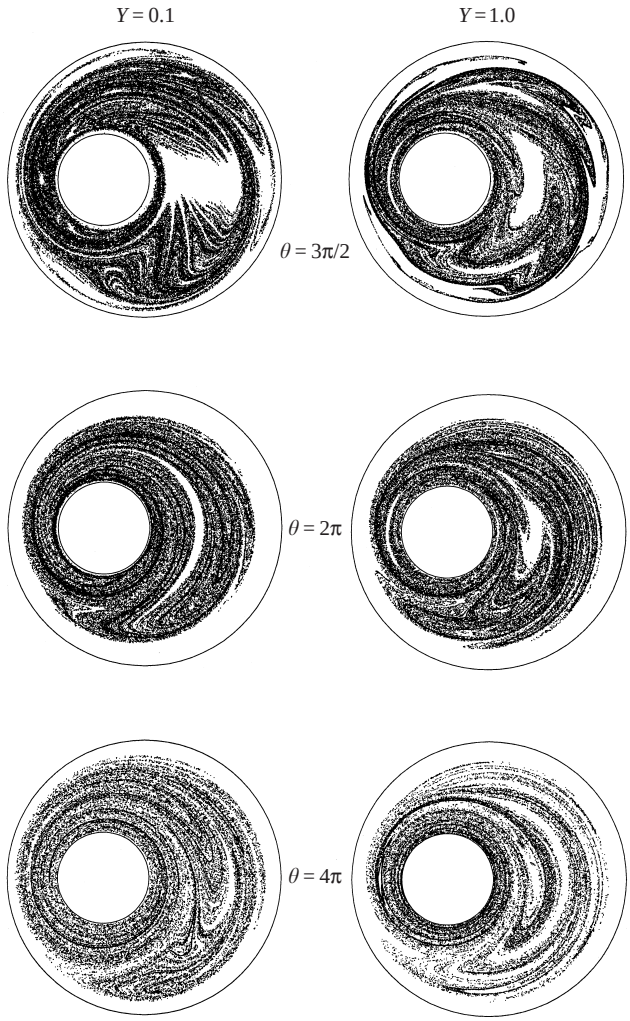

FIGURE 11. Asymptotic coverages of a passive tracer initially positioned in the middle of the small gap; after 36 rotations of the inner cylinder; configuration 1.

Note that the stretching λ depends on $\boldsymbol{F}$ as well as on the orientation of the initial vector $\mathrm{d}\boldsymbol{X}$. In addition, if $\mathrm{d}\boldsymbol{X} = \mathrm{d}X\boldsymbol{p}$, where $\boldsymbol{p}$ is randomly distributed, then $\lambda = \frac{1}{3}\mathrm{tr}\,\boldsymbol{F}^T\boldsymbol{F}$.

The details of our numerical implementation for the advection of passive tracers and for the lineal stretching can be found in Fan *et al.* (2000). Generally, due to the co-existence of regular and chaotic regions, the distribution of the stretching is highly non-uniform throughout the flow domain after several periods. Since the initial locations of 4800 tracked particles are uniform in the finite element meshes, it is convenient for us to present the distribution of stretching by plotting contours of the logarithm of λ according to their initial locations. It was observed that the final locations of these particles are roughly uniform. As a global assessment of the stretching we take the *geometric mean* over all the values of stretching tracked and

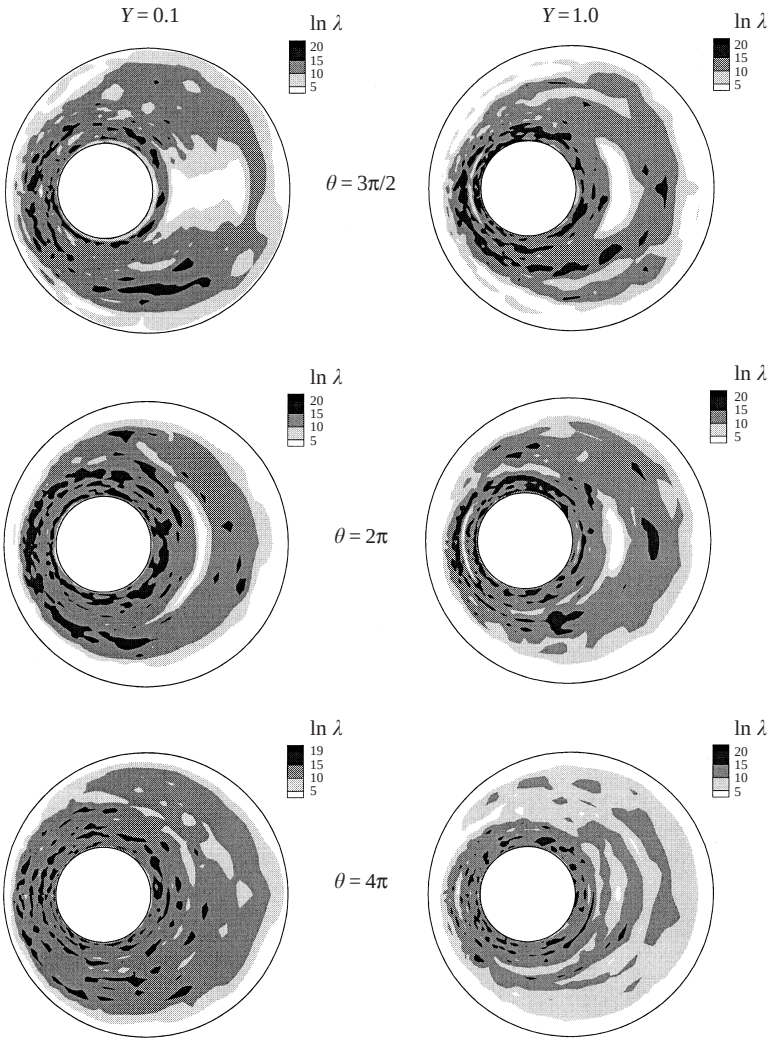

FIGURE 12. Contours of the logarithm of the lineal stretching of 4800 fluid particles initially uniformly distributed in the flow domain of configuration 1; after 36 rotations of the inner cylinder.

define the mean stretching, $\langle\lambda\rangle$, as

$$\ln\langle\lambda\rangle = \frac{1}{N}\sum_{1}^{N} \ln\lambda_i, \tag{6.5}$$

where N is the number of particles tracked and λ_i is the stretching of particle i. If a flow domain is dominated by chaotic mixing, the mean stretching is expected to increase exponentially with time.

7. Results of the mixing computation

7.1. *Configuration 1*

Figure 11 plots the asymptotic coverages of a passive tracer initially located in the middle of the small gap, after 16 periods for the rotation mode of $\theta = 3\pi/2$, 12

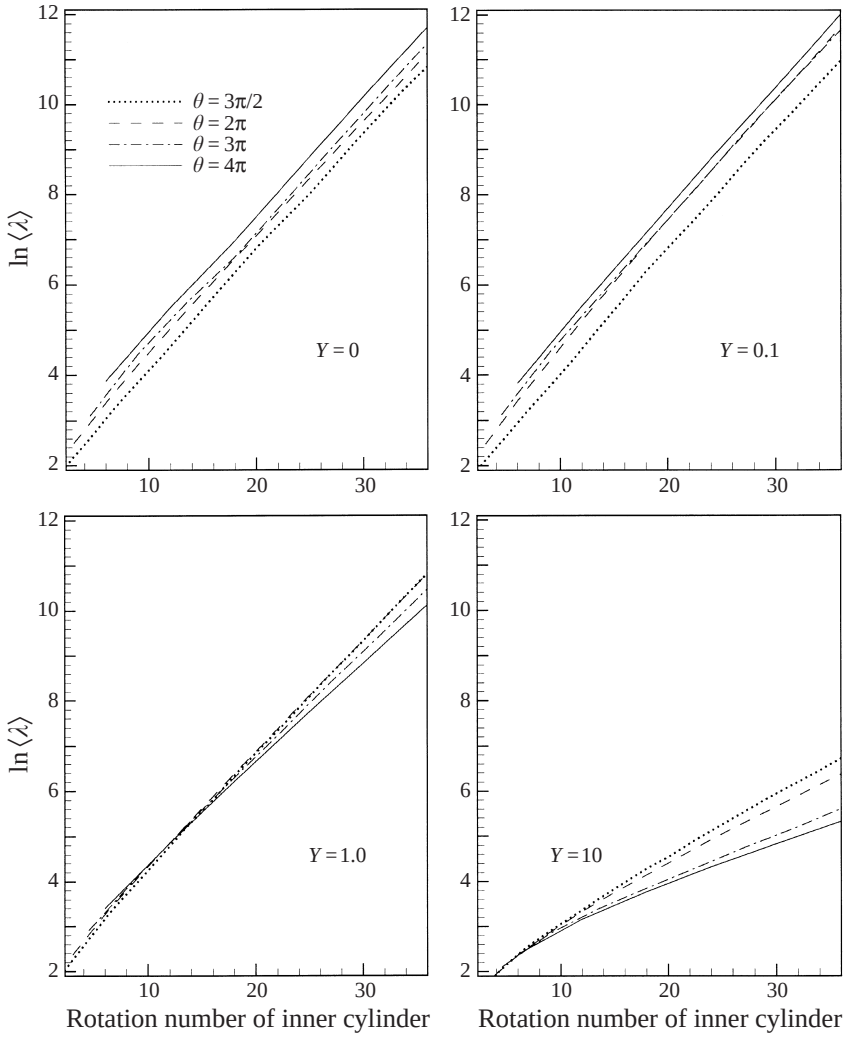

FIGURE 13. Variations of the logarithm of mean stretching with time in configuration 1.

periods for $\theta = 2\pi$ and 6 periods for $\theta = 4\pi$, respectively. The unshaded areas are the regular regions into which the tracer cannot penetrate while in the chaotic regions (black) one can detect folds and striations of the mixed tracer. For $Y = 0.1$ and $\theta = 2\pi$ the crescent-shaped island in the large gap is the same as in the experiment for Newtonian fluids reported by Swanson & Ottino (1990).

Figure 12 shows the corresponding contours of the logarithm of the lineal stretching λ. Careful comparisons show that the regions of lowest stretching are well matched in an antisymmetric way to the regular regions in figure 11, even for some tiny islands. Swanson & Ottino (1990) also found a similar phenomenon for the Newtonian fluid and they suggested that the manifold structure associated with the low-order periodic points may be responsible for the agreement between the stretching distribution and the coverage of a passive tracer.

Figure 13 shows the logarithm of the mean stretching $\langle\lambda\rangle$ versus the rotation number of the inner cylinder, including the rotation modes of $\theta = 3\pi/2$, $\theta = 2\pi$, $\theta = 3\pi$ and $\theta = 4\pi$. It is evident that, except for the case of $Y = 10$, the mean stretching increases

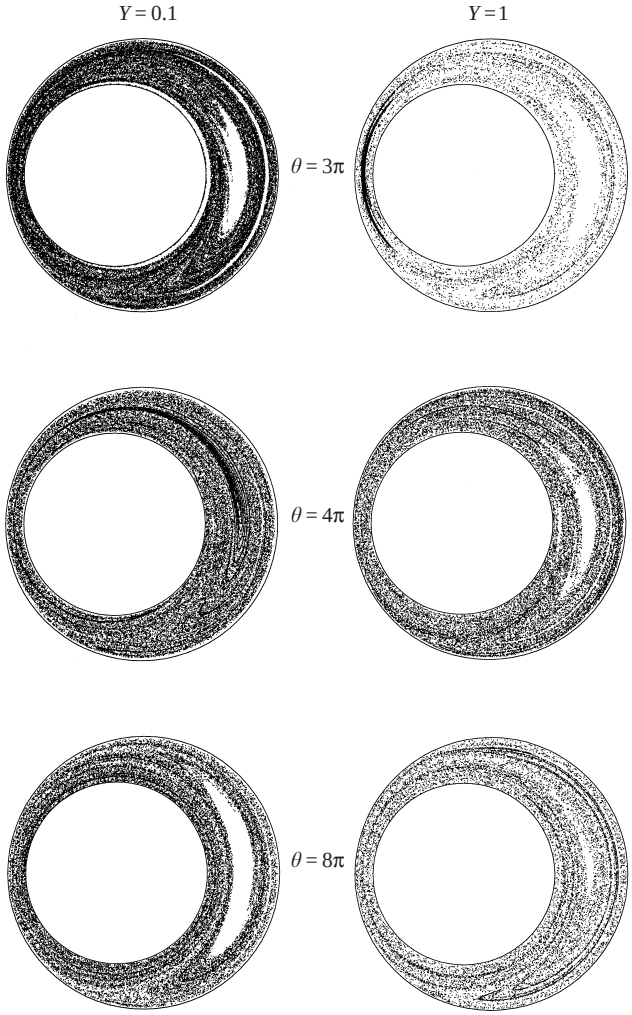

FIGURE 14. Asymptotic coverages of a passive tracer initially positioned in the middle of the small gap; after 36 rotations of the inner cylinder; configuration 2.

exponentially with time (equivalent to the rotation number of the inner cylinder). For $Y = 0$ (Newtonian) and $Y = 0.1$, the rotation mode of $\theta = 4\pi$ has the highest mean stretching. For $Y = 1.0$, the rotation mode of $\theta = 2\pi$ seems to be an optimal choice in view of figures 11, 12 and 13. As expected, the mixing of the fluid with the high yield stress $Y = 10$ is rather poor because it is dominated by large unyielded regions.

7.2. *Configuration 2*

To compare the mixing characteristics of configuration 1 ($R_i = 1,\ R_o = 3$) with those of configuration 2 ($R_i = 1,\ R_o = 1.5$), here we present results for equal total linear displacement per period; thus the rotation mode of $\theta = 3\pi$ in configuration 2 corresponds to $\theta = 3\pi/2$ in configuration 1, and $\theta = 4\pi$ in configuration 2 corresponds to $\theta = 2\pi$ in configuration 1, etc. Figures 14, 15 and 16 show the coverages of a passive tracer, the distributions of stretching in the flow domain and the variations of the mean stretching with time.

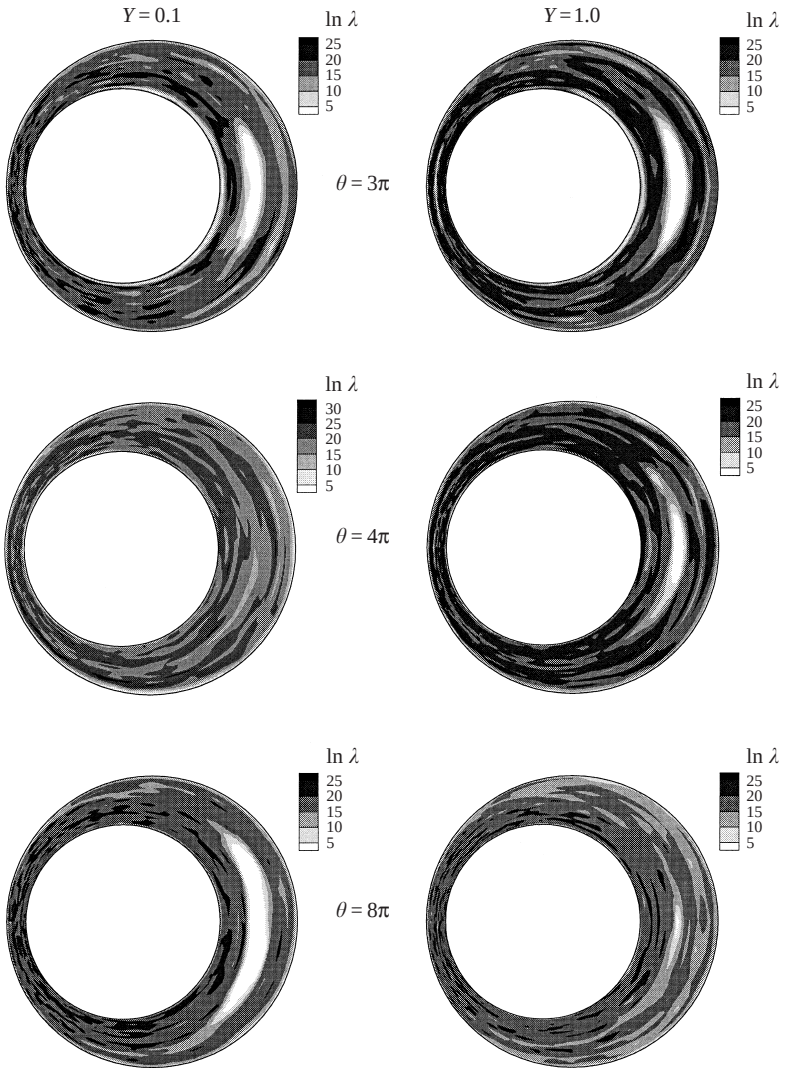

FIGURE 15. Contours of the logarithm of the lineal stretching of 4800 fluid particles initially uniformly distributed in the flow domain of configuration 2; after 36 rotations of the inner cylinder.

In figure 14, the tracer coverage in the case of $Y = 1$ and $\theta = 3\pi$ seems exceptionally light. A detailed examination reveals that, in this particular case, the tracer initially fell into a regular region in the middle of the small gap; as a result, it was trapped and not able to spread onto the major region of the flow until the sixth period; this corresponds to the presence of a narrow strip of low stretching in the middle of the small gap as shown in figure 15. Except for this accident, the agreement between the lowest-stretching regions in figure 15 and the regular regions with no tracer coverage in figure 14 is excellent. Note that the distribution of stretching is naturally consistent with the amount of mean stretching; this can be confirmed by comparing figure 15 with figure 16, and figure 12 with figure 13. Therefore plotting the distribution of stretching is a more reliable tool than plotting the coverage of a passive tracer for quantitatively assessing the advective mixing.

Through examining figure 16, it is concluded that, from $Y = 0$ to $Y = 10$, the

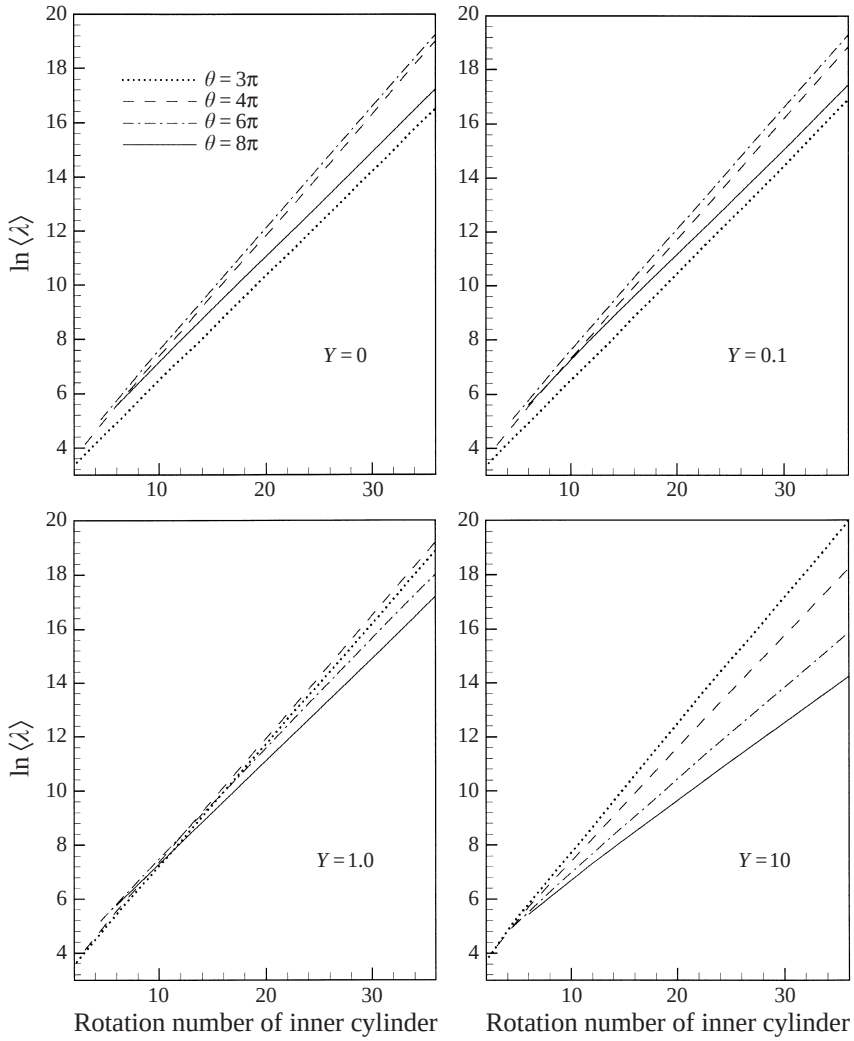

FIGURE 16. Variations of the logarithm of the mean stretching with time in configuration 2.

rotation mode of $\theta = 4\pi$ always has a relatively good performance while the choice of $\theta = 8\pi$ should be avoided. Worth noticing is that configuration 2 can provide an exponential growth of the mean stretching even for fluid with the high yield stress, $Y = 10$; in this respect it is obviously superior to configuration 1. Figure 17 compares the stretching distributions for $Y = 10$ in configuration 1 with those in configuration 2; as expected, the bulk unyielded materials in configuration 1 present a major barrier to effective mixing.

8. Mixing efficiency

Finally, we want to address the issue of engineering interest: mixing efficiency. We discuss the efficiency in terms of the mean lineal stretching as proposed by Ottino (1989):

$$e_\lambda = \frac{\mathrm{d}\ln\langle\lambda\rangle}{\mathrm{d}t}\frac{1}{\sqrt{\langle \boldsymbol{D} : \boldsymbol{D}\rangle}} \tag{8.1}$$

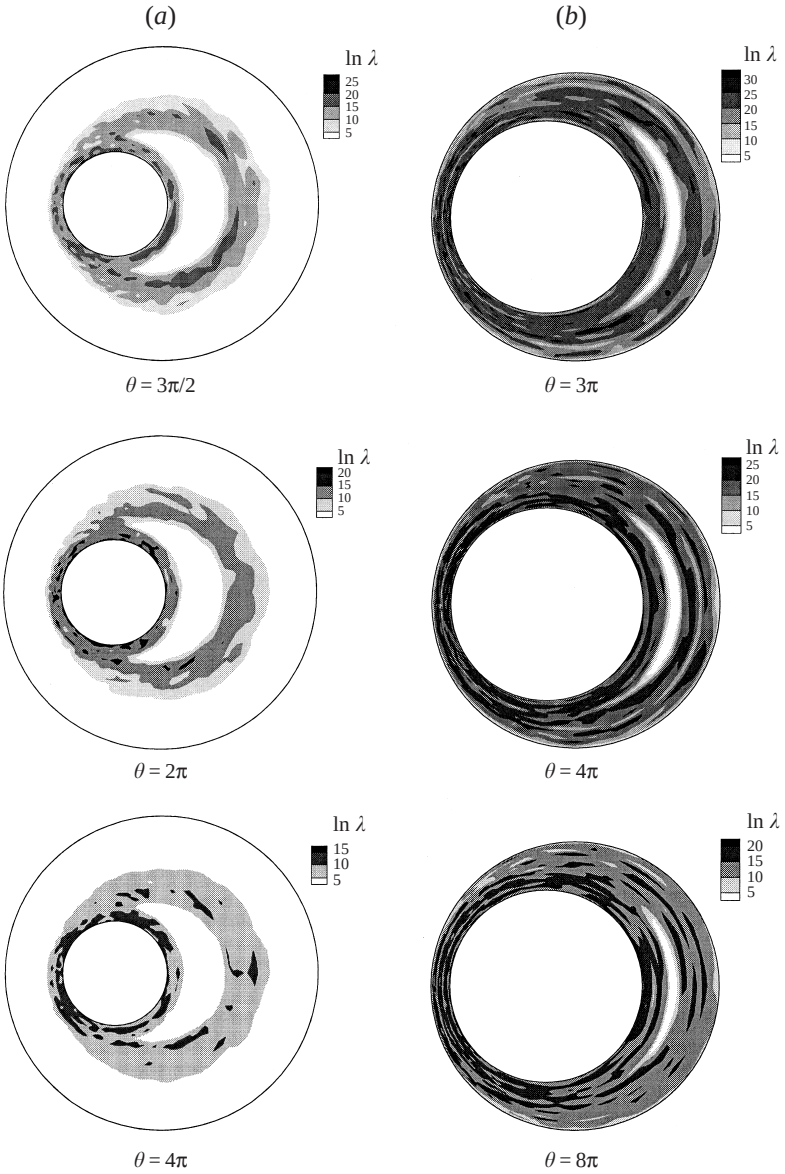

FIGURE 17. Comparison of the stretching distributions in (*a*) configuration 1 and (*b*) configuration 2; the yield stress $Y = 10$; after 36 rotations of the inner cylinder.

where $\boldsymbol{D} = (\nabla \boldsymbol{u} + (\nabla \boldsymbol{u})^T)/2$. This definition of efficiency has the advantage of being dimensionless and bounded (< 1.0), and in which $\sqrt{\langle \boldsymbol{D} : \boldsymbol{D} \rangle}$ is related to the energy dissipation for purely viscous fluids. In the present problem if *only yielded flow regions are considered*, the rate of work consumption per unit volume is (in dimensionless form, and note $\dot{\gamma} = 2\boldsymbol{D}$)

$$\boldsymbol{\tau} : \boldsymbol{D} = \left(1 + \frac{Y}{\sqrt{2(\boldsymbol{D} : \boldsymbol{D})}}\right) 2(\boldsymbol{D} : \boldsymbol{D}). \tag{8.2}$$

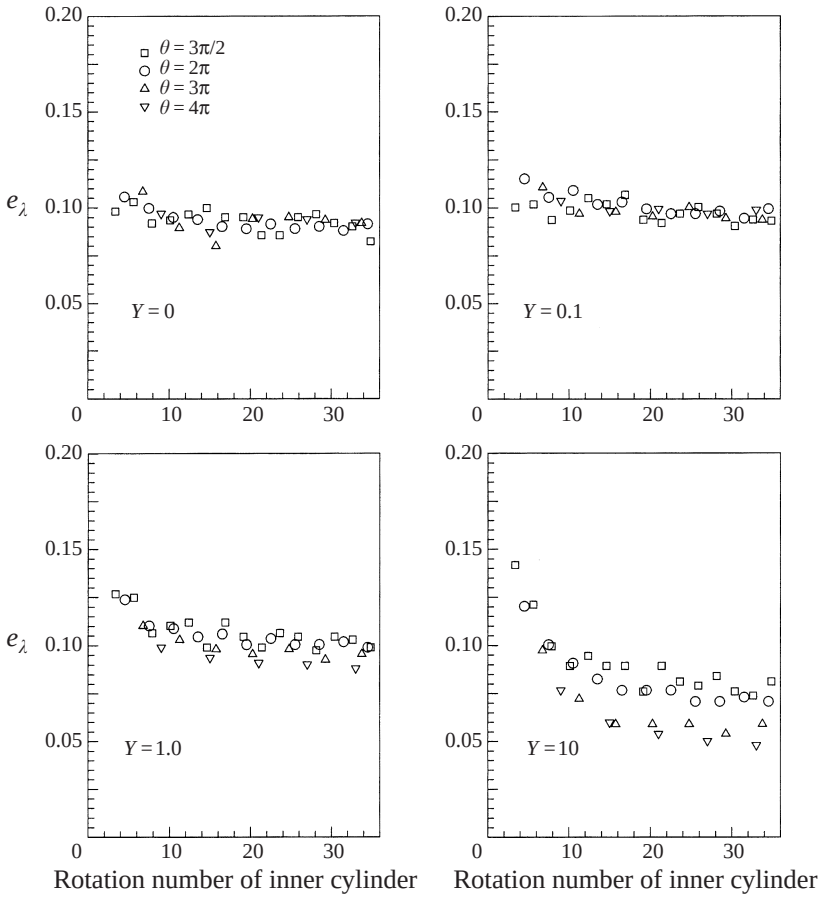

FIGURE 18. Variation of the mixing efficiency e_λ with the operation time; configuration 1.

A mean value of the rate of work consumption per unit volume can be calculated as

$$\langle \boldsymbol{\tau} : \boldsymbol{D} \rangle = (T_i \Omega_i + T_o \Omega_o)/2\pi(R_o^2 - R_i^2) \tag{8.3}$$

where T is the torque exerted on the cylinder wall, Ω is the angular velocity, the subscripts i, o stand for inner and outer cylinders, respectively. The corresponding mean value of $\sqrt{\boldsymbol{D} : \boldsymbol{D}}$ is then obtained by solving equation (8.2); the differential in (8.1) is approximated by differencing the values at the end of consecutive periods. Figures 18 and 19 show the mixing efficiencies, calculated in this way, versus the operation time for configurations 1 and 2, respectively. A common characteristic is that, up to $Y = 1.0$, the level of yield stress, as well as the rotation mode, has little effect on the mixing efficiency. At the high level of yield stress, $Y = 10$, the mixing efficiency generally is lower, especially for the rotation modes of large θ. Quite unexpectedly, the mixing efficiencies in configuration 2 are considerably lower than in configuration 1; this is attributed to the larger work consumption and much smaller area of the flow domain of configuration 2, and also to the fact that this efficiency calculation does not take into account the unyielded zones. Worth noting here is that, with configuration 2, the mixing efficiencies behave more *levelly* with time and the stretching distributions are more uniform than with configuration 1, see figures 12–19.

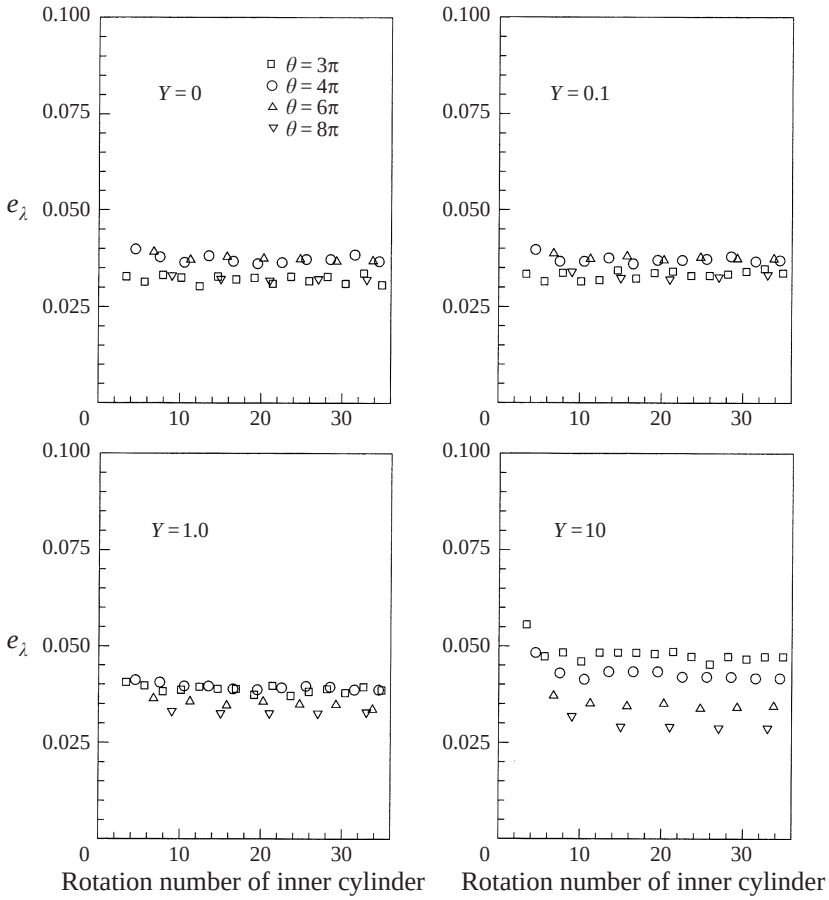

FIGURE 19. Variation of the mixing efficiency e_λ with the operation time; configuration 2.

9. Conclusions

The bi-viscosity model and Papanastasiou model smooth the yield criterion of ideal Bingham plastics, which facilitates the implementation of ordinary finite element methods in analysing complex flows of viscoplastic fluids. Instead of the yield surface, these two models predict a sharp transition from low to high viscosity. In the present flow between eccentric cylinders, the two models quantitatively agree with each other in terms of the velocity field and the practically unyielded region. Accuracy and convergence of the solutions have been demonstrated through increasing the interpolation order (the *p*-extension) and comparing with the exact solutions for the reduced case of Newtonian flows. Unlike the bi-viscosity model, the Papanastasiou model is endowed with a continuous-derivatives viscosity; consequently, it has a much larger convergence radius than the bi-viscosity model in the algorithm with Newton iteration. Therefore the computation using the Papanastasiou model is more robust and economic than that using the bi-viscosity model.

Our numerical simulations of the steady flows in two geometrical configurations show that the extent of the unyielded zones enlarges when the yield stress increases. In addition to the unyielded fluid at rest, some plugs with rigid rotation in the flows have been discovered, including rotating plugs stuck onto the outer cylinder and rotating,

even counter-rotating, plugs disconnected from both cylinders. These unyielded zones have been identified by the yield criterion of the model as well as by close examination of the velocity profiles there. As far as we are aware, these phenomena have not been previously reported in the literature; we expect further examination or confirmation from experiments.

The unsteady, periodic flow of viscoplastic fluids between eccentric cylinders was simulated by using the piecewise-steady approximation. The mixing characteristics of these flows have been studied by analysing the asymptotic coverage of a passive tracer, the final distribution of lineal stretching in the flow domain and the variation of the mean stretching with the operation time. The tracer-coverage plotting is intuitive but qualitative and, occasionally, it depends on the initial location of the tracer; on the other hand, the distribution of stretching is quantitative and more reliable in reflecting the mixing characteristics. It is interesting that the zones with the lowest stretching in the distribution graphs are remarkably well matched with the regular zones in the tracer-coverage graphs. The present numerical investigation has demonstrated that the time-periodic flows in the eccentric annuli do produce chaotic mixing for the viscoplastic fluids, except for the high yield stress, $Y = 10$, in configuration 1. The mixing characteristics and mixing efficiency of various rotation modes in two geometrical configurations have been examined in the hope of finding some general rules. It is important to realize that, for plastic fluids, a major barrier to effective mixing is the unyielded plugs in the flow, which are controlled by the yield stress and the geometrical configuration, not by the rotation mode; therefore it is expected that the geometrical configuration has a much greater impact on the characteristics and efficiency of the advective mixing than has the rotation mode.

We gratefully acknowledge the support from the Australian Research Council (ARC). Y. R. Fan also acknowledges the support of the National Natural Science Foundation of China. The computations were done on the Sydney Distributed Computing (SyDCom) Laboratory.

REFERENCES

Abdali, S. S., Mitsoulis, E. & Markatos, N. C. 1992 Entry and exit flows of Bingham fluids. *J. Rheol.* **36**, 389–407.

Aref, H. & Balachandar, S. 1986 Chaotic advection in a Stokes flow. *Phys. Fluids* **29**, 3515–3521.

Barnes, H. A. 1999 The yield stress – a review or '$\pi\alpha\nu\tau\alpha\ \rho\epsilon\iota$' – everything flows? *J. Non-Newtonian Fluid Mech.* **81**, 133–178.

Bercovier, M. & Engelman, M. 1980 A finite element method for incompressible non-Newtonian flows. *J. Comput. Phys.* **36**, 313–326.

Beverly, C. R. & Tanner, R. I. 1989 Numerical analysis of extrudate swell in viscoelastic materials with yield stress. *J. Rheol.* **33**, 989–1009.

Beverly, C. R. & Tanner, R. I. 1992 Numerical analysis of three-dimensional Bingham plastic flow. *J. Non-Newtonian Fluid Mech.* **42**, 85–115.

Bird, R. B., Dai, G. C. & Yarusso, B. J. 1983 The rheology and flow of viscoplastic materials. *Rev. Chem. Engng* **1**, 1–70.

Chaiken, J., Chu, C. K., Tabor, M. & Tan, M. 1987 Lagrangian turbulence and spatial complexity in a Stokes flow. *Phys. Fluids* **30**, 687–694.

Ellwood, K. R., Georgiou, G. C., Papanastasiou, T. C. & Wilkes, J. O. 1990 Laminar jets of Bingham-plastic liquids. *J. Rheol.* **34**, 787–812.

Fan, Y. R., Tanner, R. I. & Phan-Thien, N. 2000 A numerical study of viscoelastic effects in the chaotic mixing between eccentric cylinders. *J. Fluid Mech.* **412**, 197–225.

Franjione, J. G. & Ottino, J. M. 1987 Feasibility of numerical tracking of material lines and surfaces in chaotic flows. *Phys. Fluids* **30**, 3641–3643.

Gartling, D. K. & Phan-Thien, N. 1984 A numerical simulation of a plastic fluid in a parallel-plate plastometer. *J. Non-Newtonian Fluid Mech.* **14**, 347–360.

Kusch, H. A. & Ottino, J. M. 1992 Experiments on mixing in continuous chaotic flows. *J. Fluid Mech.* **236**, 319–348.

Lipscomb, G. G. & Denn, M. M. 1984 Flow of Bingham fluids in complex geometries. *J. Non-Newtonian Fluid Mech.* **14**, 337–346.

Muzzio, F. J., Swanson, P. D. & Ottino, J. M. 1991 The statistics of stretching and stirring in chaotic flows. *Phys. Fluids* A **3**, 822–834.

Nieckele, A. O., Naccache, M. F. & Mendes, P. R. S. 1998 Crossflow of viscoplastic materials through tube bundles. *J. Non-Newtonian Fluid Mech.* **75**, 43–54.

Niederkorn, T. C. & Ottino, J. M. 1993 Mixing of a viscoelastic fluid in a time-periodic flow. *J. Fluid Mech.* **256**, 243–268.

Niederkorn, T. C. & Ottino, J. M. 1994 Chaotic mixing of shear-thinning fluids. *AIChE J.* **40**, 1782–1793.

Ottino, J. M. 1989 *The Kinematics of Mixing: Stretching, Chaos, and Transport*. Cambridge University Press.

Papanastasiou, T. C. 1987 Flows of materials with yield. *J. Rheol.* **31**, 385–404.

Souvaliotis, A., Jana, S. C. & Ottino, J. M. 1995 Potentialities and limitations of mixing simulations. *AIChE J.* **41**, 1605–1621.

Swanson, P. D. & Ottino, J. M. 1990 A comparative computational and experimental study of chaotic mixing of viscous fluids. *J. Fluid Mech.* **213**, 227–249.

Szabo, B. & I. Babuska, 1991 *Finite Element Analysis*. John Wiley & Sons.

Walton, I. C. & Bittleston, S. H. 1991 The axial flow of a Bingham plastics in a narrow eccentric annulus. *J. Fluid Mech.* **222**, 39–60.

Wannier, G. H. 1950 A contribution to the hydrodynamics of lubrication. *Q. Appl. Maths* **8**, 1–32.